Micromagnetic Device Simulation

João Pedro Gomes Moutinho[1, 2, *]

[1]*Department of Physics, Instituto Superior Técnico, Universidade de Lisboa, Av. Rovisco Pais 1, 1049-001 Lisboa, Portugal*
[2]*INESC-MN, Rua Alves Redol 9, 1000-029 Lisboa, Portugal*

Micromagnetic devices, based on the micromagnetic model, have a large number of applications in the development of new technologies, from emerging information storage solutions like MRAMs, to sensory devices used in biomedical and industrial applications. The numerical implementation of the micromagnetic model is studied, where the two main problems are the global demagnetizing interaction and the time integration of the Landau-Lifshitz-Gilbert equation. Numerical methods for the demagnetizing field are overviewed and a new FFT based method is developed using a convolution kernel computed from a linear system discretization of the magnetostatic Poisson equation. We show this method has advantages over other FFT methods both in terms of speed and accuracy when a Yee cell discretization of Maxwell's equations is used. Furthermore, the time integration of the LLG equation is studied, where nonconservative Runge-Kutta methods were implemented alongside a semi-conservative Gauss-Seidel method and a conservative implicit mid-point method, found in literature. These methods prove to be promising options to deal with the time integration aspects of the model, sacrificing some efficiency in favour of accuracy. We conclude by presenting our work in a *Mathematica* simulation tool prepared to study spin valve devices.
Keywords: Micromagnetic Device Simulation, Numerical Methods, FFT Poisson Solver, Conservative LLG Integration, Open Source Simulation Tool.

I. INTRODUCTION

Over the past few decades the transition to the digital world has lead to an exponential growth in the requirements of information storage, both in terms of capacity and access speed. Magnetic materials have long been the focus of considerable research due to their wide range of technological applications. Not only are they found in mass magnetic storage, but also in sensing devices, magnetic stripes on credit cards and magnetic ink for character recognition used in the banking industry to process and clear documents.

One of the first applications of the principles of ferromagnetism in the area of magnetic storage was the Ferrite Core Memory, initially tested in 1952 with the IBM 405 Alphabetical Accounting Machine. For the next 20 years, before semiconductor memories were introduced in the 1970s, the ferrite core memory was the main form of random-access memory. Magnetic storage, of course, did not end with the ferrite core memory. The now widely used hard-drives of desktop computers are a very well-known example of high capacity magnetic storage. A ferrite core memory chip in 1965 had dimensions in the order of centimeters with a storage capacity of only 4×10^3 bits. A common hard disk found today in a laptop computer has about the same size and can store more than 1 terabyte of data, or roughly 8×10^{12} bits! In fact, devices and binary structures for modern recording and sensing technology are made of magnetic media with dimensions in the order of micro to nanometers — often referred to as micromagnetic devices.

The micromagnetic device development group at INESC-MN specializes in magnetoresistive devices with biomedical and industrial sensory applications [1–4], having also worked with magnetic storage focused devices [5, 6]. The process of developing these devices has a lot of stages and decisions that must be made in terms of layout, design rules, and nanofabrication. It is thus very common to resort to computer simulations to assist this process. These simulations must be reliable so that underneath all the complex interactions in the device the results can be trusted to match the physical reality of the system, and must be efficient not only to allow more device configurations to be tested in less time, but also to allow more complex systems to be simulated with the available computer power.

There has been constant interest in developing faster and more robust numerical methods for the computational implementation of the micromagnetic model. Previous codes have been developed at INESC-MN with this purpose [7], although they are now mostly outdated. Currently the experimental group uses the simulation software *SpinFlow3D*, however this is a closed-source tool that has already stopped receiving support from its creators, and online resources have been shut down. Similar motivations have lead other researchers to create fully-featured open-source micromagnetic simulation tools such as *OOMMF* [8], *MuMax*^{3} [9], *magnum.fe* [10] and *MicroMagnum* [11], ready to be used by experimentalists. Some of these were also tested during the course of this thesis and considered as an option to be used by INESC-MN.

The main focus of this thesis will be the treatment of the demagnetizing field problem and the numerical integration of the LLG equation, while also working towards the improvement of the current situation with regards to micromagnetic simulations at INESC-MN.

*Electronic address: joao.p.moutinho@gmail.com

We will start by introducing the main interactions of the micromagnetic model and their discretization, followed by study of the two aforementioned problems. As a conclusion to our work we will introduce a *Mathematica* simulation tool we developed to study spin valve devices.

II. THE MICROMAGNETIC MODEL

A. Micromagnetic Free Energy

The theory of micromagnetics stands upon a continuous magnetization framework. For a given magnetic body occupying a region $\Omega \subseteq \mathbb{R}^3$ we consider the average magnetization at location $\mathbf{r} \in \Omega$ to be characterized by the vector field $\mathbf{M}(\mathbf{r})$ [A/m] which, for a dynamical situation, can also be a function of time,

$$\mathbf{M} = \mathbf{M}(\mathbf{r},\, t). \tag{1}$$

This framework treats both short and long range interactions in terms of the free energy of the magnetic body, a functional of the magnetization field $\mathbf{M}$, presented in Eq. 4. We have considered the four main micromagnetic interactions in the functional: Exchange, Anisotropy, Demagnetizing and Zeeman, described in the following paragraphs.

The key interaction in ferromagnetic materials is the exchange interaction. These materials are known to present a very strong spontaneous magnetization of the order of the saturation magnetization M_s due to the alignment of neighbouring spins. This suggests ferromagnets should have small uniformly magnetized regions, called magnetic domains. Weiss [12] postulated the existence of these domains and defined the behaviour of the magnetization magnitude along the ferromagnetic material as being simply a function of temperature and equal to the saturation magnetization, $M_s = M_s(T)$, thus separating the direction and magnitude of the magnetization vector field,

$$\mathbf{M}(\mathbf{r},\, t) = M_s\, \mathbf{m}(\mathbf{r},\, t). \tag{2}$$

In 1931 Heisenberg theoretically justified Weiss's theory describing the exchange interaction on the basis of quantum theory [13], and in 1935 Landau and Lifshitz [14] proposed a mathematical approach to this interaction with the introduction of a term in the free energy to penalize magnetization disuniformities.

Secondly, the anisotropy interaction accounts for the energy-favored directions of the magnetization in ferromagnetic bodies, produced by the lattice structure of each material and certain crystal symmetries. The most common case is for ferromagnetic materials to have uniaxial anisotropy, meaning there exists only one easy direction, or easy axis $\mathbf{u}_{\text{an}}$.

The demagnetizing interaction accounts for the long-range interactions of magnetic moments within the material. At each position in the magnetic body a demagnetizing field is felt with a contribution from the whole magnetization distribution. The demagnetizing field $\mathbf{H}_{\text{d}}$ is described by the magnetostatic case of Maxwell's equations [15],

$$\nabla \cdot \mathbf{H}_{\text{d}} = -\nabla \cdot \mathbf{M} \quad \text{and} \quad \nabla \times \mathbf{H}_{\text{d}} = 0, \tag{3}$$

with an appropriate energy contribution.

Finally an extra Zeeman term can be added to the free energy functional to account for the introduction of an externally applied field $\mathbf{H}_{\text{ext}}$. Summing the energy contribution of each interaction we obtain the free energy functional 4,

$$\begin{aligned} G[\mathbf{M},\, \mathbf{H}_{\text{ext}}] &= F_{\text{ex}}[\mathbf{M}] + F_{\text{an}}[\mathbf{M}] + F_{\text{demag}}[\mathbf{M}] + G_{\text{ext}}[\mathbf{M},\, \mathbf{H}_{\text{ext}}] \\ &= \int_\Omega \left[A_{\text{ex}} (\nabla \mathbf{m})^2 - K_1 \left(\mathbf{u}_{\text{an}} \cdot \mathbf{m}\right)^2 - \frac{1}{2}\mu_0 \left(\mathbf{M} \cdot \mathbf{H}_{\text{d}}\right) - \mu_0 \left(\mathbf{M} \cdot \mathbf{H}_{\text{ext}}\right) \right] d^3 r, \end{aligned} \tag{4}$$

where A_{ex} is the exchange constant with dimensions of [J/m] and K_1 is the first order anisotropy constant with dimensions of [J/m^3].

B. Micromagnetic Equilibrium

The equilibrium configuration of magnetization arises from minimizing the free energy functional with the restriction that $\|\mathbf{M}(\mathbf{r})\| = M_s$. We thus consider that the first-order variation δG vanishes for any variation $\delta \mathbf{m}$ of the unit-vector field $\mathbf{m}$,

$$\delta G = G[\mathbf{m} + \delta \mathbf{m}] - G[\mathbf{m}] = 0, \tag{5}$$

where we have the constraint $\|\mathbf{m} + \delta \mathbf{m}\| = 1$. Applying the first order variation to each energy term individually and imposing the sum to vanish leads to the set of equations 6,

$$\mathbf{m} \times \mathbf{H}_{\text{eff}} = 0, \qquad \left.\frac{\partial \mathbf{m}}{\partial \mathbf{n}}\right|_{\delta\Omega} = 0, \tag{6}$$

where we have defined the effective field $\mathbf{H}_{\text{eff}}$,

$$\mathbf{H}_{\text{eff}}(\mathbf{r}) \equiv -\frac{1}{\mu_0 M_s}\frac{\delta G}{\delta \mathbf{m}} = \mathbf{H}_{\text{ex}} + \mathbf{H}_{\text{an}} + \mathbf{H}_{\text{d}} + \mathbf{H}_{\text{ext}}. \tag{7}$$

The effective field incorporates a field formulation to represent the exchange and anisotropy interactions in

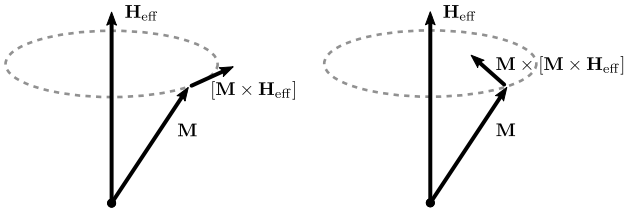

FIG. 1: Separation of the dynamical motion of a single magnetization vector in its two main components: precession and damping, respectively.

the model,

$$\mathbf{H}_{\text{ex}} = \frac{2A_{\text{ex}}}{\mu_0 M_s}\nabla^2\mathbf{m}, \quad \mathbf{H}_{\text{an}} = \frac{2K_1}{\mu_0 M_s}(\mathbf{m}\cdot\mathbf{u}_{\text{an}})\mathbf{u}_{\text{an}}. \quad (8)$$

Equations 6 are the so-called Brown's equations which are used to determine the equilibrium configuration of magnetization within a ferromagnetic body. However, Brown's equations only describe the necessary condition for the system to be in equilibrium, but give no information as to how the system arrives at such state. To complete this description of the micromagnetic model, we must introduce the dynamical equations that describe the time evolution of the magnetization under the influence of an effective field.

C. Dynamic Equations

Research on magnetization dynamics so far has mostly been focused on the dynamical model proposed by Landau and Lifshitz [14] in 1935,

$$\frac{\partial\mathbf{M}}{\partial t} = -\gamma\mathbf{M}\times\mathbf{H}_{\text{eff}} - \frac{\lambda}{M_s}\mathbf{M}\times(\mathbf{M}\times\mathbf{H}_{\text{eff}}), \quad (9)$$

where $\gamma = 2.21\times10^5\,\text{m}\,\text{A}^{-1}\,\text{s}^{-1}$ is the electron gyromagnetic ratio. The first term in the equation represents a conservative (hamiltonian) motion. In order to treat energy dissipations Landau and Lifshitz proposed the introduction of a phenomenological torque effectively pushing the magnetization in the direction of the effective field, characterized by the phenomenological constant $\lambda > 0$. A scheme of the type of motion described by Eq. 9 is represented in Fig. 1.

In 1955 Gilbert [16] used a Lagrangian formulation to derive the conservative Landau-Lifshitz equation, introducing a phenomenological damping through a "viscous" force proportional to the time derivative of the magnetization,

$$\frac{\partial\mathbf{M}}{\partial t} = -\gamma\mathbf{M}\times\mathbf{H}_{\text{eff}} + \frac{\alpha}{M_s}\mathbf{M}\times\frac{\partial\mathbf{M}}{\partial t}, \quad (10)$$

where α is a small positive damping constant. Equation 9 is usually referred to as the Landau-Lifshitz-Gilbert (LLG) equation, and can be shown to be mathematically equivalent to Eq. 10,

$$\frac{\partial\mathbf{M}}{\partial t} = -\frac{\gamma}{1+\alpha^2}\mathbf{M}\times\mathbf{H}_{\text{eff}} - \frac{\gamma\alpha}{(1+\alpha^2)M_s}\mathbf{M}\times(\mathbf{M}\times\mathbf{H}_{\text{eff}}). \quad (11)$$

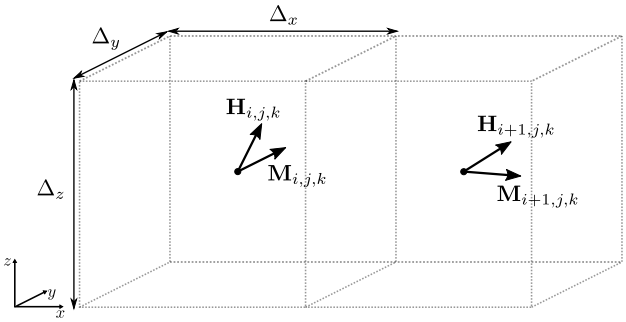

FIG. 2: Center-vector grid discretization. Every cell has the three components of each vectorial quantity discretized at the center.

III. NUMERICAL IMPLEMENTATION

In this section we will discuss the general considerations of our numerical implementation of the model, where we use a finite-difference discretization scheme. For a certain unidimensional function $f(x)$ discretized in steps of size h, the derivatives related to positions x and $x \pm h$, corresponding to the cells with index i and $i \pm 1$, are given by finite differences,

$$\frac{\partial f(x+\frac{h}{2})}{\partial x} \approx \frac{f_{i+1} - f_i}{h} + \mathcal{O}(h), \quad (12)$$

$$\frac{\partial^2 f(x)}{\partial x^2} \approx \frac{f_{i+1} - 2f_i + f_{i-1}}{h^2} + \mathcal{O}(h^2), \quad (13)$$

Note that the first derivative approximation in Eq. 12 is a forward-shifted center-difference in the sense that, since it requires the values at positions i and $i+1$, the obtained derivative is evaluated for the midway position $i+\frac{1}{2}$, corresponding to $f(x+\frac{h}{2})$, which must be stored in a different grid shifted by $h/2$. The second derivative 13 uses cells $i+1$, i and $i-1$, and so the value is stored in cell i of the same grid.

A. The Discrete Micromagnetic Model

All static interactions must come together under the Landau-Lifshitz-Gilbert equation 11. Its spatial discretization consists in discretizing the continuous fields $\mathbf{M}(\mathbf{r})$ and $\mathbf{H}_{\text{eff}}(\mathbf{r})$. The LLG equation verifies $\|\mathbf{M}(\mathbf{r},\,t)\| = M_s$, and so we must be able to verify this condition after discretization. We must also be able to perform the mathematical cross product between $\mathbf{M}$ and $\mathbf{H}_{\text{eff}}$ at each location in space. This two considerations require $\mathbf{M}$ and $\mathbf{H}_{\text{eff}}$ to be discretized on the same grid without separating the three components of each vector field. We thus define our main discretization of Ω as a three dimensional grid of $N = N_x + N_y + N_z$ cuboid cells where each cell has the vectors $\mathbf{M}_{i,j,k}$ and $(\mathbf{H}_{\text{eff}})_{i,j,k}$ at its center. This is the usual construction under which the micromagnetic model is discretized, and will be referred to as the center-vector grid, exemplified in Fig. 2.

Regarding the discretization of each static term introduced, we will start with the exchange interaction.

Following the discussion in [17], various formulations can be considered, however the most common is to apply a 7 point stencil to the Laplace operator, which is simply the three dimensional extension of Eq. 13,

$$(\mathbf{H}_{\rm ex})_{i,j,k} = \frac{2A_{\rm ex}}{\mu_0 M_s}\left[\frac{\mathbf{m}_{i+1,j,k}+\mathbf{m}_{i-1,j,k}}{\Delta_x^2} + \frac{\mathbf{m}_{i,j+1,k}+\mathbf{m}_{i,j-1,k}}{\Delta_y^2} + \frac{\mathbf{m}_{i,j,k+1}+\mathbf{m}_{i,j,k-1}}{\Delta_z^2} - \mathbf{m}_{i,j,k}\left(\frac{2}{\Delta_x^2}+\frac{2}{\Delta_y^2}+\frac{2}{\Delta_z^2}\right)\right]. \tag{14}$$

A reformulation of the free energy contribution [17] then allows us to discretize the analytical integral as

$$F_{\rm ex} = -\frac{1}{2}\mu_0 M_s \sum_{i,j,k} (\mathbf{m}\cdot\mathbf{H}_{\rm ex})_{i,j,k}\,\Delta_x\Delta_y\Delta_z. \tag{15}$$

The anisotropy interaction has a free energy contribution and a field contribution to the effective field with no dependence on magnetization derivatives, and are thus straightforward to discretize,

$$F_{\rm an} = -K_1 \sum_{i,j,k} (\mathbf{m}_{i,j,k}\cdot\mathbf{u}_{\rm an})^2\,\Delta_x\Delta_y\Delta_z\,, \tag{16}$$

$$(\mathbf{H}_{\rm an})_{i,j,k} = \frac{2K_1}{\mu_0 M_s}(\mathbf{m}_{i,j,k}\cdot\mathbf{u}_{\rm an})\mathbf{u}_{\rm an}. \tag{17}$$

The discretization of the exchange and anisotropy terms we presented is consistent with the spatial discretization requirements of the LLG equation. The demagnetizing interaction from Eqs. 3, on the other hand, is more troublesome. Since $\mathbf{H}_{\rm d}$ has zero curl, we can write it as the gradient of a certain scalar potential, $\mathbf{H}_{\rm d} = -\nabla\mathcal{V}$. We can also introduce a fictitious magnetic charge density, $\rho_{\rm M}(\mathbf{r}) = -\nabla\cdot\mathbf{M}$, allowing Eqs. 3 to be represented as a single Poisson equation,

$$\nabla^2\mathcal{V}(\mathbf{r}) = -\rho_{\rm M}(\mathbf{r}). \tag{18}$$

These equations represent a global interaction, and their solution is the most resource intensive static calculation in micromagnetic modelling. We will discuss the solution to this problem in detail in the next section, however we can now analyze how the relations from Eqs. 3 and 18 behave on a discrete grid. When we consider $\mathbf{M}$ and $\mathbf{H}_{\rm d}$ discretized according to the center-vector grid formulation, as shown in Fig. 2, the application of the divergence and curl operators in their finite-difference form becomes problematic: the first derivatives 12 in each operator impose a different grid change in each component of $\mathbf{M}$ and $\mathbf{H}_{\rm d}$. For example, in the case of the divergence operator, the x, y and z components of $\nabla\cdot\mathbf{M}$ are stored in different grids, and thus the three derivatives cannot be directly summed as a localized divergence.

In order to verify Maxwell's equations on a discrete cuboid grid each component of $\mathbf{M}$ and $\mathbf{H}_{\rm d}$ should in fact be discretized along the borders of the grid, as illustrated in Fig. 3. This is the usual approach in the Finite-Difference Time-Domain (FDTD) method

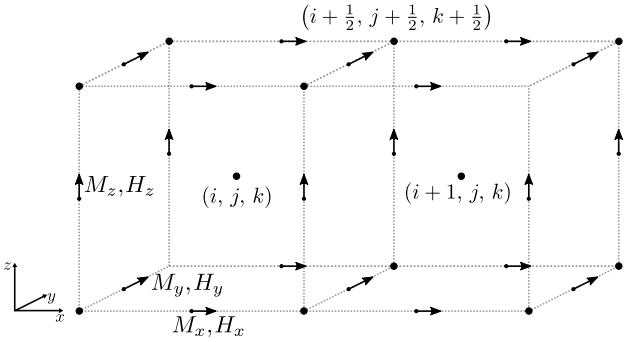

FIG. 3: Conjugate-dual grid discretization, or Yee's Grid [18], used in the FDTD method. Grid dimensions are as shown in Fig. 2.

in computational electrodynamics, as described initially by Yee [18]. In this construction, which we refer to as the conjugate-dual grid, the three derivatives from the divergence operator are stored at the vertices of the cells, which we call the conjugate grid, and the cross-derivatives from the curl operator are evaluated at the surfaces of the main grid. The discretization of the Poisson equation 18 is also consistent and this equation acts only on the conjugate grid. We will consider the notation $N'_{x,y,z} = N_{x,y,z} + 1$, where the conjugate grid has a total of $N' = N'_x + N'_y + N'_z$ cells. Finally, when we apply the gradient operator to the scalar potential $\mathcal{V}$, the finite-difference reasoning of the first derivatives lead the resulting field $\mathbf{H}_{\rm d}$ to be again organized in the borders of the main grid.

The conjugate-dual grid construction allows us to study and develop numerical methods to solve the demagnetizing field while focusing on the conservation of Maxwell's relations. However, as we have seen, this discretization is not consistent with the requirements of the LLG equation, and the demagnetizing field contribution to the effective field must still be accounted for in the center-vector grid discretization from Fig. 2. Magnetization and field averages were used in order to conciliate the two discretizations and transfer information from one grid to the other.

The most common way to address the discretization problem of the demagnetizing field in micromagnetic modelling is, in fact, to use only the center-vector grid with a tensor convolution method that transforms $\mathbf{M}$ directly in $\mathbf{H}_{\rm d}$. This method has been validated by comparison with analytical solutions and experi-

mental results [19], however it is unclear whether it conserves Maxwell's relations in a consistent manner. Other publications that use the scalar potential and averaging techniques between grids [19–21] also give no special attention dedicated to the conservation of the Maxwell's equations in their discrete form.

The free energy contribution of the demagnetizing interaction is straightforward to discretize in the center-vector grid as

$$F_{\text{demag}} = -\frac{1}{2}\mu_0 \sum_{i,j,k} \left(\mathbf{M}\cdot\mathbf{H}_{\text{d}}\right)_{i,j,k} \Delta_x\Delta_y\Delta_z, \qquad (19)$$

which also represents the discretization of the Zeeman energy contribution in Eq. 4 for an externally applied field $\mathbf{H}_{\text{ext}}$ organized in the center-vector grid.

As a final remark on the numerical implementation of the model, we set the physical constants M_s, A_{ex}, γ and $\mu_0/2$ to unity. These normalizations lead the simulation units to be defined as the following set of natural units:

Length $\rightarrow$	$\sqrt{2A_{\text{ex}}/\mu_0 M_s^2}$	Field $\rightarrow$	M_s
Time $\rightarrow$	$1/\gamma M_s$	Energy $\rightarrow$	$A_{\text{ex}}\sqrt{2A_{\text{ex}}/\mu_0 M_s^2}$

TABLE I: Natural units used during the simulation.

IV. DEMAGNETIZING FIELD

Being a global interaction, the demagnetizing field is by far the most resource intensive static calculation — the value in each cell of discretized space has a contribution of every single cell in the material. Finding ways to optimize this calculation is of great interest in the field of micromagnetics. In this section we present our approach to the problem, where we use the notation of the normalized fields $\mathbf{m}$ and $\mathbf{h}_{\text{d}}$.

Regarding Eqs. 3 and 18, the transformations of $\mathbf{m}$ into ρ_{m} and $\mathcal{V}$ into $\mathbf{h}_{\text{d}}$ are direct applications of the divergence and gradient operators, which scale with $\mathcal{O}(N)$. We are left with transforming ρ_{m} into $\mathcal{V}$, for which we need to find an efficient and reliable solver. The integral solution to Eq. 18 can be written as

$$\mathcal{V}(\mathbf{r}) = \frac{1}{4\pi}\int_{\Omega} \frac{1}{\|\mathbf{r}-\mathbf{r}'\|}\rho_{\text{m}}(\mathbf{r}')\, d^3r'. \qquad (20)$$

This integral solution has important convolution properties which we will discuss later. The difference from the well known electrostatic Poisson problem arises from the fact that the magnetic charges we are referring to are simply a mathematical construction from the divergence of the magnetization, leading to some discussion on how the surface of the magnetized material should be treated. The usual approach is to assume the distribution $\mathbf{m}(\mathbf{r})$ inside a magnetized region Ω falls suddenly to zero at the surface $\partial\Omega$. Such a perfectly defined boundary would lead to an infinite divergence at the surface, requiring an effective surface charge distribution $\sigma_{\text{m}}(\mathbf{r}) = \mathbf{m}\cdot\mathbf{n}$ to be defined [15] with an extra contribution to the potential,

$$\mathcal{V}(\mathbf{r}) = \frac{1}{4\pi}\int_{\Omega} \frac{\rho_{\text{m}}(\mathbf{r}')}{\|\mathbf{r}-\mathbf{r}'\|}\, d^3r' + \frac{1}{4\pi}\oint_{\partial\Omega} \frac{\sigma_{\text{m}}(\mathbf{r}')}{\|\mathbf{r}-\mathbf{r}'\|}\, d^2r'. \qquad (21)$$

These surface charges, however, do not exist. Instead in our approach we considered the surface to be an uncertainty region over which the magnetization changes, with its thickness effectively defined by the cell size used in the discretization, and we do not include this surface contribution. We know there is no actual discontinuity in a physical magnetization distribution, and as long as the field $\mathbf{h}_{\text{d}}$ obtained conserves the discrete Maxwell equations, we know the mathematical solution obtained for $\mathcal{V}$ is reliable.

A. Direct Poisson Discretization

By discretizing the Laplace operator directly in Eq. 18, similarly to what was done in Eq. 14, we built a linear system of equations that we must solve to find the potential in all the simulation cells,

$$\boldsymbol{A}\mathbf{x} = \mathbf{b}. \qquad (22)$$

Matrix $\boldsymbol{A}$ is essentially the discrete Laplace operator in matrix form [22], $\mathbf{x}$ is a list of the $\mathcal{V}_{i,j,k}$ unknowns, and $\mathbf{b}$ includes both the values $\rho_{i,j,k}$ and the boundary conditions for the potential. Usually, Eq. 18 is solved by setting the open boundary condition that the potential decays to zero at infinity. In order to represent this condition we used a multipole expansion, as seen in Jackson [15], to calculate the potential at some far away boundary of cells, from which we then solved the linear set of equations through a Krylov method to find the potential in all the interior cells.

With the demagnetizing scalar potential computed for all the cells, the next step is to calculate

$$\mathbf{h}_{\text{d}} = -\nabla\mathcal{V} \qquad (23)$$

and verify if the resulting field satisfies Maxwell's equations 3. In this regard, we used the function

$$f_{\text{prec}}(x_1, x_2) = -\log_{10}\left(\frac{|x_1 - x_2|}{\max\{|x_2|\}}\right) \qquad (24)$$

to estimate the accuracy of the Maxwell equalities at each location in space. Equation 24 gives the approximate number of digits that are equal between two given values x_1 and x_2. We considered a global relative comparison to $\max\{|x_2|\}$ to avoid the division operation to diverge for small local values of x_2.

We proceeded by simulating a unit cube with (N_x, N_y, N_z) varying between $\{16, 32, 48, 64\}$, and calculated $\mathbf{h}_{\text{d}}$ considering a random magnetization in each cell. We calculated the derivatives in both Maxwell's equations 3 as finite-differences for all the

simulation cells, where we recall the discrete organization of the vector fields presented in Fig. 3. We then used the difference values at each appropriate position as x_1 and x_2 to calculate the respective value from Eq. 24 and verify the four equalities that can be specified from Maxwell's equations 3. Averaging the results over all the simulation cells, the divergence equality was satisfied with an 8 digit precision and the three curl equalities were satisfied with a 16 digit precision. While we obtained a much better precision for the curl equation, this is only dependent on a correct application of the gradient operator to any given scalar potential. However, having also obtained a good precision for the divergence equation, we can conclude that the linear system method is a reliable procedure to calculate the scalar potential, and thus obtain a physically accurate demagnetizing field.

B. FFT Convolution Method

The linear system approach to Poisson's equation, and consequently, the demagnetizing field proved to be very reliable in the conjugate-dual grid discretization. Currently, however, the demagnetizing field in most simulations is calculated through a FFT convolution method, taking advantage of the well known convolution theorem. FFTs scale with $\mathcal{O}(N \log_2 N)$, and this is usually faster than linear system methods. The main advantage of this method is that the geometrical information of the system needed for Eq. 20 is only calculated once and stored in a *kernel*, independently of the magnetization distribution present. As mentioned the integral solution 20 to Poisson's equation has convolution properties,

$$\mathcal{V}(\mathbf{r}) = (G * \rho)(\mathbf{r}), \tag{25}$$

where $G(\mathbf{r}-\mathbf{r}') = \frac{1}{4\pi\|\mathbf{r}-\mathbf{r}'\|}$ is the Green's function for the Laplace operator, acting as a kernel that only depends on geometrical properties. In discretized space integral 20 is replaced by a sum which represents a discrete convolution, and so a discrete kernel that correctly represents the continuous convolution must be computed. The kernel G in Eq. 25 is a scalar, however most FFT methods used in this problem consider the surface charge contribution from Eq. 21, which allows for some convenient mathematical manipulations. Knowing that $\rho = -\nabla \cdot \mathbf{m}$ and $\mathbf{h}_\mathrm{d} = -\nabla\mathcal{V}$, two equivalent forms of 21 can be written:

$$\mathcal{V}(\mathbf{r}) = \frac{1}{4\pi}\int_\Omega \mathbf{m}(\mathbf{r}') \cdot \nabla_{\mathbf{r}'} \frac{1}{\|\mathbf{r}-\mathbf{r}'\|}\, d^3r', \tag{26}$$

$$\mathbf{h}_\mathrm{d}(\mathbf{r}) = -\frac{1}{4\pi}\nabla_{\mathbf{r}} \int_\Omega \mathbf{m}(\mathbf{r}') \cdot \nabla_{\mathbf{r}'} \frac{1}{\|\mathbf{r}-\mathbf{r}'\|}\, d^3r'. \tag{27}$$

Equation 26 is obtained by applying the divergence theorem to the surface contribution in Eq. 21 and joining the two contributions as volume integrals. Equation 27 is simply the gradient of Eq. 26. The two integrals can be described as the convolutions $(\mathbf{S}*\mathbf{m})(\mathbf{r})$ and $(\tilde{\mathbf{N}}*\mathbf{m})(\mathbf{r})$, where the kernel $\mathbf{S}$ is a vector and the kernel $\tilde{\mathbf{N}}$ is a tensor. For finite-difference implementations both were discretized assuming uniformly magnetized cuboids with the respective integrals then solved analytically from that approximation: $\tilde{\mathbf{N}}$ in [23] and $\mathbf{S}$ more recently in [21].

The demagnetizing tensor convolution 27 is the most commonly used method for the solution of the demagnetizing field, implemented in well known simulations [8, 9, 11]. The vector convolution method 26 has more recently been implemented in [11]. Considering our approach to the discretization of Maxwell's equations, the latter is of more interest to our study because it also solves the scalar potential at the vertices of the simulation cells, allowing us to test its reliability in the conjugate-dual grid from Fig. 3. The tensor method, on the other hand, transforms $\mathbf{m}$ into $\mathbf{h}_\mathrm{d}$ directly using only the center-vector grid from Fig. 2, and so we cannot verify if the results satisfy the discretization of Maxwell's equations we employ.

Our main focus, however, is in the convolution from Eq. 25, since we do not wish to consider the surface charge contribution. While Berkov *et al.* [20] uses a kernel that acts on the charge density, the publication is not explicit on how to calculate it. McMichael *et al.* [24] refer to this kernel as being calculated numerically, and only treat the 2D case. As mentioned, $\mathbf{S}$ and $\tilde{\mathbf{N}}$ were discretized assuming uniformly magnetized cuboids, and so we proceeded to discretize G by assuming uniformly *charged* cuboids. Both of these assumptions can be justified by the exchange interaction. Following the same logic of the analytical integration of $\mathbf{S}$ in [21], we found that the analytical integration of G can be done similarly to the work of Hummer [25] in the context of molecular dynamics, who performed an analytical integration of the electrostatic potential for a unit cube. We adopted the notation G_a for this approximation since we will introduce another version of G.

Regardless, after implementing the FFT convolution method with both $\mathbf{S}$, according to its publication [21], and G_a, we were unable to match the precision results we obtained with the linear system method. Both kernels produced errors in Maxwell's divergence equation as high as 10% in cells near the borders of the material. While the introduction of the surface charge contribution in the integral 21 would be a natural reason to justify this loss in precision, the fact that the potential solution obtained from G_a was also unreliable suggests the constant magnetization and constant charge approximations used in the analytical kernel integrations may also be at fault. This shortcoming motivated us to take a different approach to the FFT convolution method, which we will now introduce.

1. *A Numerical Approach to the Scalar Kernel*

The idea behind this method is to extract a kernel numerically from a linear system calculation that efficiently replicates the solutions of the linear system

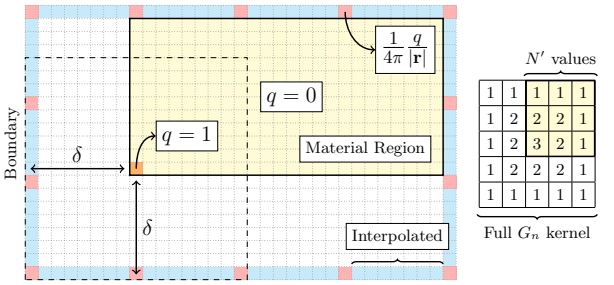

FIG. 4: Scheme of the considerations used to calculate the numerical scalar kernel G_n.

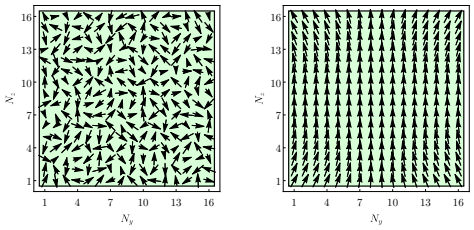

(a) Random State. (b) Flower State.

FIG. 5: Vertical cut through the center magnetized cube discretized in a $16 \times 16 \times 16$ grid with both a random magnetization distribution and a flower state distribution.

method to a given system. We adopted the notation G_n for this numerical kernel. In the next few steps we describe in the procedure we developed to expedite the computation of G_n, aided by the scheme we present in Fig. 4 where we highlight some key points.

1. A single unit charge is considered in the first corner cell of the conjugate grid.
2. The boundaries of the conjugate grid are extended so that they are at least at a distance δ from the charged cell, where δ will be referred to in multiples of the largest cell dimension: $\delta = 32 \Leftrightarrow \delta = 32 \times \max\{\Delta_x, \Delta_y, \Delta_z\}$.
3. The boundary conditions are calculated through a monopole approximation for selected cells, interpolating the rest.
4. The potential $\mathcal{V}$ is solved for all the interior cells of the box through the linear system method.
5. Given the single unit charge, the values of $\mathcal{V}$ inside the conjugate grid of the material region can be used directly for the kernel. This corresponds to N' kernel values.
6. The full G_n kernel with dimensions $(2N'_x - 1, 2N'_y - 1, 2N'_z - 1)$ is obtained by filling the values of the remaining cells according to the symmetries illustrated on the right of Fig. 4.

As with the other kernels, this is a one-time calculation for each geometry. The reciprocal kernel $\mathcal{F}\{G_n\}$ can then be stored in memory and every single scalar potential calculated afterwards for that geometry only requires a discrete 3D FFT of the charge density, a point wise product in reciprocal space, and a discrete inverse 3D FFT of the reciprocal space potential, yielding the real space potential,

$$\mathcal{V} = \mathcal{F}^{-1}\{\,\mathcal{F}\{G_n\} \cdot \mathcal{F}\{\rho\}\,\}. \tag{28}$$

As we will see, we can use the δ parameter we just introduced to fine-tune the precision of this kernel.

2. *Kernel Accuracy and Efficiency*

So far we have talked about various methods to solve the demagnetizing field problem in magnetostatics. In order to compare them with more detail we started by simulating a cubic magnetic particle with side $L = 50\,\text{nm}$ discretized in a cubic grid $n \times n \times n$ for $n = \{16, 32, 64\}$. We considered a random and a flower state of magnetization, as shown in Fig. 5.

The first aspect that should be commented is the efficiency of each of the FFT convolution methods. Even though we did not include the widely used demagnetizing tensor $\tilde{\mathbf{N}}$ in our study, an efficiency comparison between $\mathbf{S}$ and $\tilde{\mathbf{N}}$ was done in [21]. The conclusion was that performing a convolution with $\mathbf{S}$ was about 1.5 times faster, mostly because $\mathbf{S}$ reduced the number of inverse FFTs from three to one, at the cost of only one extra gradient operation. The reciprocal space calculation was also reduced from a tensor-vector product to a vector-vector product. With the scalar kernels G_a or G_n, compared to both $\tilde{\mathbf{N}}$ and $\mathbf{S}$, we also reduced the the number of direct FFTs from three to one, maintained only one inverse FFT, and further reduced the reciprocal space calculation to a scalar product. This came at the cost of one extra divergence operation, but like the gradient, it scales with $\mathcal{O}(N)$. The increase in performance is clear, and in our calculations the convolutions with the scalar kernels G_a and G_n performed about 1.5 to 2 times faster than those with the vector kernel $\mathbf{S}$.

More importantly, we must compare the reliability aspects. In table II we present the precision results of the demagnetizing field solution obtained from each method, as calculated from Eq. 24 applied to the divergence equation $\nabla \cdot \mathbf{h}_\text{d} = -\nabla \cdot \mathbf{m}$. We included both the average precision value over all the cells as well as the value for the cell with minimum precision. The curl equation was once again satisfied with close to 16 digit precision, as was expected since in all cases the field obtained was a gradient of a scalar potential, and we immediately see the linear system method maintained the good precision results that we first obtained in section IV A. The analytical kernels $\mathbf{S}$ and G_a were calculated from uniform magnetization and charge density approximations, respectively, which are physically based around the existence of the exchange interaction. As expected, these approximations do not perform well for the case of random magnetization since such a distribution does not fit the micromagnetic model, and we see both $\mathbf{S}$ and G_a yield very low precision values for the random state.

		Divergence Equation Precision ($\langle \#_{\text{digits}} \rangle$, Eq. 24)									
		LS		G_a		**S**		$G_{n,32}$		$G_{n,64}$	
	Grid	Min	Av.	Min	Av.	Min	Av.	Min	Av.	Min	Av.
Random	16^3	8.18	8.83	0.45	1.29	0.33	1.22	7.63	8.43	8.06	8.64
	32^3	8.23	8.90	0.45	1.33	0.33	1.24	5.76	6.67	7.75	8.40
	64^3	8.22	8.79	0.45	1.35	0.30	1.24	5.57	6.55	7.01	8.83
Flower	16^3	7.97	8.56	0.56	2.57	0.88	3.07	6.73	8.33	8.09	9.71
	32^3	7.80	8.54	0.58	3.51	0.90	4.01	4.49	6.37	7.75	8.53
	64^3	7.24	7.88	0.59	4.62	0.91	5.01	4.36	6.29	6.99	8.00

TABLE II: Reliability comparison between the four demagnetizing field methods: linear system method (LS) and three convolution methods with the analytical kernel G_a, analytical kernel **S** and numerical kernel G_n for $\delta = \{32, 64\}$.

For a physical distribution such as the flower state, on the other hand, we see the average precision is much better and increases with the grid size. Nevertheles, we still found cells at the boundary of the material, where the divergence of the magnetization is greater, to maintain low precision values. This suggests either the surface charge effects or the constant charge and magnetization approximations become unreliable in these outter regions. With the scheme we developed to approximate the scalar kernel G_n numerically we could recreate the precision results obtained with the linear system method, with high precision values in both the average over all the cells as well as the minimum precision cell. Furthermore, we see a clear precision increase when we change $\delta = 32$ to $\delta = 64$.

We thus show that the FFT convolution method with the scalar kernel G_n is not only faster than other FFT convolution methods, but can also guarantee a demagnetizing field solution that is reliable over the whole simulation grid using a Yee cell discretization.

3. *Standard Problem #4*

So far we have used the precision of Maxwell's equations as an important factor in comparing the kernels, but when we deal with magnetization dynamics we must average the field components to the center of the cells due to the discretization requirements of the LLG equation, as shown in Fig. 2, and so we must also validate our method in this aspect. For this purpose we solved the standard problem #4 commonly used to compare micromagnetic simulations, as described in [26]. In Fig. 6 we present the results obtained, where we plot the time evolution of the average magnetization components for the first case of the external field mentioned in [26]. We used a discretization of $256 \times 64 \times 2$ cells, and calculated the time integration of the LLG equation 11 with a 4th order Runge Kutta method. While some small deviations can be observed, these are not uncommon between the various solutions so far submitted to the μMAG website. The dynamical behaviour of the problem while using the scalar kernel G_n for the computation of the demagnetizing field follows the same oscillation pattern, thus completely validating our static calculations.

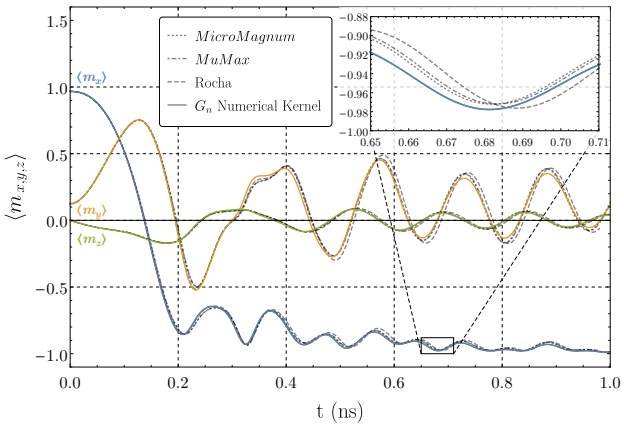

FIG. 6: Time evolution of the average magnetization components according to the Standard Problem #4 [26]. Results obtained with the scalar kernel G_n were compared with the ones computed with the simulation codes *MuMax* [9] and *MicroMagnum* [11], as well as the previous data submitted by Rocha [27] to the μMag site [28].

In conclusion, our kernel provides very good efficiency and precision results in the conjugate-dual grid scheme, and is able to reproduce the known standard problem #4 results in the center-vector grid discretization. We reduced the number of needed FFTs when compared to other kernels in literature and also included a simple fine-tuning mechanism for the precision in the form of the parameter δ. Furthermore, the computation of this kernel is not based on any physical approximation, producing similar reliability of results indepedently of the physical significance of the magnetization distribution, making the method more mathematically robust.

V. MAGNETIZATION DYNAMICS

With the numerical calculation of the demagnetizing field optimized, we can efficiently obtain the effective magnetic field correspondent to each magnetization distribution. The dynamical aspects of the magnetization under such an effective magnetic field can be described by the LLG equation 11. The numerical

treatment of this equation has proved to be a complicated task. On one hand it is extremely non-linear, and on the other hand it includes two types of motion that act on different time scales: a very fast precession and a very slow damping. The most common way to address this problem is to use general purpose integrators, like Runge-Kutta methods, which are implemented in well known simulation tools [9, 11]. These explicits methods however do not conserve the physical properties of the LLG equation and so a very small time step must be used to correctly mimic the complex LLG motion. Extensive work has been invested into developing integration methods specific to the LLG equation to try and overcome this problem [29, 30].

A discussion on the physical properties of the LLG equation, regarding both norm and energy conservations can be found in [30], where a conservative mid-point integration method was developed. For the purpose of this section, we implemented a 4th order Runge-Kutta (RK) method [22], a semi-implicit Gauss-Seidel (GS) method [29] and the aforementioned fully implicit mid-point (MP) method [30].

The implementation of the RK method is straightforward. The GS method, on the other hand, requires equations of the screened Poisson type,

$$\left[\nabla^2 - \lambda^2\right] v(\mathbf{r}) = -u(\mathbf{r}), \tag{29}$$

to be solved at each iteration. For this purpose we adapted our work from section IV and implemented a FFT convolution solver for these equations. The implementation of the MP method uses a quasi-Newton procedure which requires a large linear system of equations to be solved at each iteration, where we used the Krylov method previously used in section IV A.

Our initial objective for this chapter was to overcome the time step constraints of traditional Runge Kutta methods by approaching the time integration with more problem specific methods. However, after implementing the different integrators for the LLG equation, we found that by increasing the time step a strange numerical noise would propagate itself in the simulation and lead the magnetization to diverge to an anti-parallel state, or anti-ferromagnetic state, over the whole domain. Further tests lead us to conclude this noise only manifested itself in the presence of the exchange interaction, and we found our code is not the only one to display this behaviour [31], although there are other codes that do not have this problem [9]. Regardless, for a small enough time step, we were able to recover the known standard problem #4 results with the RK, GS and MP methods that we have already shown in Fig. 6.

Given that we found the noise propagation to be independent of the LLG integration method used and demagnetizing field calculation, to be only related to the exchange field calculation, and since we have obtained the known results of the standard problem #4 with all the methods tested for a small time step, we can conclude both the GS method and the MP method were correctly implemented according to their publications [29, 30]. Furthermore, we can conclude the noise propagation must be related to the numerics of the base equations, which we have narrowed down to

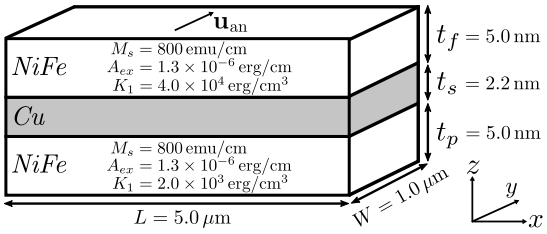

FIG. 7: Basic spin valve configuration. We consider a pinning field of $\mathbf{H}_{\text{pin}} = 200\,\mathbf{e}_y$ Oe. The easy axis $\mathbf{u}_{\text{an}}$ is also along the y direction for both layers (CGS units).

$$\frac{\partial \mathbf{m}}{\partial t} = \mathbf{m} \times \nabla^2 \mathbf{m}. \tag{30}$$

The numerical implementation of this equation must require some subtle treatment, which we did not test, and may prove to be an interesting exercise in numerical analysis for future work.

VI. SPIN VALVE SIMULATION

The ultimate goal of our work is for these simulations to be used in parallel with experimental tests to optimize the development of micromagnetic devices at INESC-MN. We thus followed the work Mendes [7], who had previously worked on the simulation of spin valve devices at INESC-MN, in order to build a simple *Mathematica* tool for the simulation of these devices.

A simple spin valve structure which we will use as an example is presented in Fig. 7. For the bottom pinned layer we model the pinning effect through an external field $\mathbf{H}_{\text{pin}}$. Furthermore we do not explicitly model the spacer layer, and include both a magnetostatic coupling effect and an interlayer exchange coupling between the free and the pinned layer. The magnetostatic coupling is discussed in [7] and the exchange coupling in [9], where we have included two adimensional constants n_{d} and n_{ex}, respectively, to tune the desired strength of each coupling.

With the introduction of the pinning effect, the magnetostatic coupling and the exchange coupling, each term has a respective energy contribution to the total energy of the system that we included in the micromagnetic model. The interest in spin valves is to study how the magnetization distributions in the layers vary with a certain external field, and so we included a conjugate gradient method based on the work of Berkov *et al.* [20] to find equilibrium states of magnetization for a given applied field.

We considered a discretization grid with $200 \times 40 \times 2$ cells, using one vertical cell for each layer. In his work Mendes reports an average magnetostatic coupling strength of 50 Oe and exchange coupling strength of 20 Oe, and we estimated that by setting $n_{\text{d}} = 5 \times 10^{-3}$ and $n_{\text{ex}} = 1.6 \times 10^{-3}$ we could reproduce the same coupling. For extended use, these parameters should

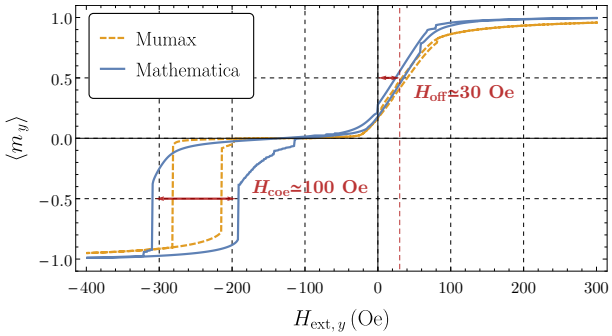

FIG. 8: Transfer curve of the average magnetization along the y axis for the spin valve of figure 7, simulated both in our *Mathematica* tool as well as MuMax.

be calibrated experimentally. The transfer curve of the spin valve in Fig. 7 was obtained with the simulation of a full field sweep between 300 Oe and −400 Oe along the y axis and sweeped in steps of 1 Oe. In Fig. 8 we present the transfer curve of the average magnetization component $\langle m_y \rangle$, averaged over the whole spin valve. The results we obtained for the transfer curve in figure 8 are very similar to both the results of Mendes [7] and to the MuMax simulation. The differences observed can be justified with the differences in the demagnetizing field method used, as we have already discussed in section IV. The difference in the hysteresis of the pinned layer can also be correlated to the fact that we use an energy minimization algorithm and MuMax uses a dynamic integration of the LLG equation to relax the system, which is less prone to find local energy minima that trap the magnetization.

VII. CONCLUDING REMARKS

In this work we have overviewed the basic micromagnetic model and its numerical treatment with the focus on the simulation of micromagnetic devices. We have presented new FFT convolution method for the demagnetizing field which has advantages over other methods found in literature both in terms of performance and precision, conserving Maxwell's equations when a Yee cell discretization is used. We have also shown this method recovers the known standard problem #4 results when the field is transfered to the usual center-vector discretization used in micromagnetics. Furthermore, we have developed a simple spin valve simulation tool in *Mathematica* to be used at INESC-MN. This tool allows for different spin valve structures to be studied with varied materials and parameters. More importantly, it consists of a single *Mathematica* file organized with a modular approach. The compact code is very easy to read and modify, and this structure allows for future interactions to be implemented with relative ease, which we have found to be a lacking feature in the currently available open-source codes.

[1] D. Leitao, A. Silva, R. Ferreira, E. Paz, F. Deepack, S. Cardoso, and P. Freitas, Journal of Applied Physics **115**, 17E526 (2014).
[2] P. Coelho, D. C. Leitao, J. Antunes, S. Cardoso, and P. P. Freitas, IEEE Trans. Magn **50** (2014).
[3] J. P. Valadeiro, J. Amaral, D. C. Leitão, R. Ferreira, S. F. Cardoso, and P. J. Freitas, IEEE Transactions on Magnetics **51**, 1 (2015).
[4] R. Macedo, F. Cardoso, S. Cardoso, P. Freitas, J. Germano, and M. Piedade, Applied Physics Letters **98**, 103503 (2011).
[5] A. V. Silva, D. C. Leitao, Z. Huo, R. J. Macedo, R. Ferreira, E. Paz, F. L. Deepak, S. Cardoso, and P. P. Freitas, IEEE Transactions on Magnetics **49**, 4405 (2013).
[6] J. Yang, R. J. Macedo, M. G. Debs, R. Ferreira, S. Cardoso, P. J. Freitas, J. M. Teixeira, and J. O. Ventura, IEEE Transactions on Magnetics **46**, 2002 (2010).
[7] M. Mendes, *Micromagnetic Simulations of Spin Valve devices*, Master's thesis, Instituto Superior Técnico (2005).
[8] M. J. Donahue and D. G. Porter, "OOMMF User's guide." US Department of Commerce, Technology Administration, National Institute of Standards and Technology (1999).
[9] A. Vansteenkiste, J. Leliaert, M. Dvornik, M. Helsen, F. Garcia-Sanchez, and B. Van Waeyenberge, Aip Advances **4**, 107133 (2014).
[10] C. Abert, L. Exl, F. Bruckner, A. Drews, and D. Suess, Journal of Magnetism and Magnetic Materials **345**, 29 (2013).
[11] "MicroMagnum," `http://micromagnum.informatik.uni-hamburg.de`.
[12] P. Weiss, J. phys. theor. appl. **6**, 661 (1907).
[13] W. Heisenberg, Z. Physik **69**, 287 (1931).
[14] L. D. Landau and E. M. Lifshitz, Phys. Z. Sowiet **8**, 101 (1935).
[15] J. D. Jackson, *Classical Electrodynamics* (Wiley, 1999).
[16] T. L. Gilbert, Physical Review **100**, 1243 (1955).
[17] M. J. Donahue and D. G. Porter, Physica B: Condensed Matter **343**, 177 (2004).
[18] K. Yee, IEEE Transactions on antennas and propagation **14**, 302 (1966).
[19] B. Van de Wiele, F. Olyslager, L. Dupré, and D. De Zutter, Journal of Magnetism and Magnetic Materials **322**, 469 (2010).
[20] D. V. Berkov, K. Ramstöcck, and A. Hubert, physica status solidi (a) **137**, 207 (1993).
[21] C. Abert, G. Selke, B. Kruger, and A. Drews, IEEE Transactions on Magnetics **48**, 1105 (2012).
[22] W. H. Press, S. A. Teukolsky, W. T. Vetterling, and B. P. Flannery, *Numerical Recipes in C*, Vol. Vol. 2 (Cambridge University Press, 1996).
[23] A. J. Newell, W. Williams, and D. J. Dunlop, Journal of Geophysical Research: Solid Earth **98**, 9551 (1993).
[24] R. McMichael, M. Donahue, D. Porter, and J. Eicke, J. Appl. Phys **85**, 111 (1999).
[25] G. Hummer, Journal of electrostatics **36**, 285 (1996).
[26] "Standard Problem 4," `http://http://www.ctcms.nist.gov/~rdm/std4/spec4.html`.
[27] T. Rocha, *Dynamic Micromagnetic Simulations*, Master's thesis, Instituto Superior Técnico (2008).
[28] "μMAG – Micromagnetic Modeling Activity Group," `http://www.ctcms.nist.gov/~rdm/mumag.org.html/`.
[29] C. J. García-Cervera and W. Ee, IEEE transactions on magnetics **39**, 1766 (2003).
[30] M. d'Aquino, C. Serpico, and G. Miano, Journal of Computational Physics **209**, 730 (2005).
[31] R. Zhu, arXiv preprint arXiv:1501.07293 (2015).